Tellus (1991), *43A*, 266–274

Bifurcations in a barotropic low-order model with self-interaction

By R. J. HAARSMA and J. D. OPSTEEGH, *Royal Netherlands Meteorological Institute, P.O. Box 201, 3730 AE DE BILT, The Netherlands*

(Manuscript received 2 January 1990; in final form 3 January 1991)

ABSTRACT

For finite equivalent depth, the shallow-water equations (SWE) exhibit instabilities based on dyad interactions. This process is called self-interaction. In the present paper, we investigate how the stationary states of a low-order spectral model based on the SWE on the sphere are affected by self-interaction. This is done by computing the bifurcation diagram for increasing strength of the forcing in one of the vorticity components. The instabilities occurring in this low-order system are topographic instability and self-interaction. Self-interaction generates saddle-node as well as Hopf bifurcations, resulting in multiple steady-states and limit cycles. For large values of the forcing, self-interaction significantly affects the steady-state curve originating from topographic instability. Extrapolating these results to the real atmosphere, self-interaction may influence the atmosphere's nonlinear behavior.

1. Introduction

In Haarsma and Opsteegh (1988), the stability properties of the shallow-water equations (SWE) were investigated. In that paper, we demonstrated the existence of an instability mechanism, called self-interaction, which originates from dyad interactions. For infinite equivalent depth ($H_e \to \infty$), in which case the SWE reduce to the barotropic vorticity equation (BVE), this instability process vanishes.

In their pioneering study Charney and DeVore (1979) demonstrated the existence of multiple steady states due to saddle-node bifurcations in a low-order model containing topographic instability only. Since then, many studies have been devoted to the analysis of nonlinear low-order models in which various types of instability occur. Topographic instability was combined with either baroclinic instability (Charney and Straus, 1980; Reinhold and Pierrehumbert, 1982) or barotropic instability (Legras and Ghil, 1985; Källén, 1981).

In this paper, we combine topographic instability with self-interaction. We are interested in the following two questions: what type of bifurcations occur in a model with self-interaction only and what is the effect of self-interaction on the bifurcation diagram that originates from topographic instability? The latter question is inspired by studies of Reinhold and Pierrehumbert (1982) and others, who showed that the bifurcation diagram due to a single instability mechanism can be drastically changed when a new instability mechanism is introduced.

In Haarsma and Opsteegh (1988), we discussed the relevance of the SWE for the large-scale low-frequency motion in the atmosphere. The SWE describe the horizontal structure of a stratified flow, like the atmosphere, only when the nonlinear advection terms are small. So they are probably too simple to study all aspects of the lower frequencies in the atmosphere. Nevertheless the choice of a finite equivalent depth is probably more realistic than simply assuming that $H_e \to \infty$, in which case the SWE reduce to the frequently studied BVE. If this is true, then self-interaction might be a relevant process for the large-scale low-frequency motion in the atmosphere.

In Section 2 we describe the low-order spectral model. A short explanation of self-interaction is presented in Section 3. In Section 4, we present the bifurcation diagram when self-interaction is the only instability mechanism. For a model with topographic instability and self-interaction we discuss its bifurcation diagram in Section 5, followed by the conclusions and a discussion of the results in Section 6.

2. Model

The nondimensional SWE on a rotating sphere, including forcing, dissipation and topography are given by:

$$\frac{\partial \zeta}{\partial t} = -\boldsymbol{V}\cdot\nabla(\zeta + f) - (\zeta + f)\,D + G_{\mathrm{f}} - \varepsilon\zeta, \tag{1a}$$

$$\frac{\partial D}{\partial t} = -\nabla^2\left(\phi + \frac{\boldsymbol{V}\cdot\boldsymbol{V}}{2}\right) - \nabla\cdot[\boldsymbol{k}\times\boldsymbol{V}(\zeta + f)] - \varepsilon D, \tag{1b}$$

$$\frac{\partial \phi}{\partial t} = -\boldsymbol{V}\cdot\nabla(\phi - \phi_{\mathrm{h}}) - (\phi - \phi_{\mathrm{h}})\,D - \frac{D}{F}, \tag{1c}$$

where ζ, D and ϕ are the relative vorticity, horizontal divergence and perturbation geopotential respectively, ϕ_{h} is the geopotential of the topography, f the planetary vorticity, $\boldsymbol{V}$ is the horizontal velocity field, $\boldsymbol{k}$ the vertical unit vector and G_{f} the vorticity forcing. The vorticity as well as the divergence equation contain a Rayleigh friction term with friction parameter ε.

The non-dimensional variables involved in (1) are defined as follows:

$$\zeta = \zeta^*/\Omega, \qquad D = D^*/\Omega, \qquad \phi = \phi^*/a^2\Omega^2,$$
$$t = t^*\Omega, \qquad f = f^*/\Omega, \tag{2}$$

where a and Ω are the radius and angular velocity of the earth respectively. The asterisks denote the dimensional variables. The only nondimensional parameter in (1) is Lamb's parameter:

$$F = \frac{a^2\Omega^2}{gH_{\mathrm{e}}}, \tag{3}$$

where H_{e} is the equivalent depth and g is gravity. As shown in Haarsma and Opsteegh (1988) the SWE reduce to the BVE in the limit $F \to 0$.

For convenience we rewrite (1c) as:

$$\frac{\partial \phi}{\partial t} = -\boldsymbol{V}\cdot\nabla\left(\phi - \frac{\eta}{F}\right) - \phi D - (1 - \eta)\frac{D}{F}, \tag{1d}$$

where $\eta = \phi_{\mathrm{h}}^*/(gH_{\mathrm{e}})$ is the topography scaled by the equivalent depth.

We express the variables of (1) in a series of spherical harmonics. The expansion is truncated at a certain wavenumber, thereby reducing the set of three partial differential equations to a finite set of $3N$ nonlinear ordinary differential equations, where N is the number of spectral components retained in the truncation. We have only considered the asymmetric components in the vorticity and the symmetric components in the divergence and geopotential, thereby excluding cross equatorial flow. The special form of truncation we have chosen in the different experiments will be outlined in the description of each experiment. For all experiments, the Rayleigh friction ε is $1.90\ 10^{-6}\ \mathrm{s}^{-1}$, which corresponds to an e-folding time of 6 days.

3. Self-interaction

In this section, we will give a short review of self-interaction. A more extensive treatment can be found in Boyd (1983a, b) and in Haarsma and Opsteegh (1988). The normal modes of the SWE are Hough functions (Longuet-Higgins, 1968). For $F = 0$, they reduce to spherical harmonics, which are the normal modes of the BVE. The spherical harmonics are exact solutions of the nonlinear BVE, but for $F > 0$ the normal modes of the linear SWE are not exact solutions of the nonlinear SWE. So they decay without the necessity of being perturbed. The decay is such that a single Hough mode γ generates a secondary Hough mode β. This is called self-interaction.

In general, self-interaction is weak and the decay of a Hough mode is slow compared to the decay rates resulting from barotropic instability by wave triads. So Hough modes can be considered approximate solutions of the nonlinear SWE. However when the phase speed of the primary Hough mode equals that of its secondary mode, the decay into that mode is fast. This is called self-resonance.

We distinguish two types of self-resonance:

(1) second Harmonic Resonance: occurs when the phase speed of the primary wave with zonal wave number m_γ equals that of its second harmonic component ($2m_\gamma$);

(2) long-wave/short-wave resonance: occurs for stationary primary Hough modes. They decay into zonal flow components.

This definition of self-interaction is different from Benzi et al. (1986). They studied an equivalent barotropic model of a quasi-geostrophic flow confined to a β channel. According to their definition self-interaction occurs when for a chosen orthonormal set of expansion functions $\{g_n\}$ of the streamfunction ψ:

$$\psi(x, y, t) = \sum_n A_n(x, t)\, g_n(y),$$

the integral

$$\delta = \int g_n^2\, g_{nyyy}\, \mathrm{d}y \neq 0.$$

They showed that when the integral is unequal to zero an extra term $\delta A_n A_{nx}$ appears in the time evolution equation for A_n which describes the interaction of g_n onto itself. According to their definition self-interaction thus depends on the choice of the expansion functions. This is not true for the concept of self-interaction as defined in the present paper. We have defined it in terms of the normal modes of the shallow-water equations, which are not dependent on the particular choice of the expansion functions.

4. Bifurcations due to self-interaction

In this section, we investigate what type of bifurcations occur due to self-interaction. We choose $F = 2.75$, which corresponds to an equivalent depth of $8 \cdot 10^3$ m for the atmosphere. The restriction to self-interaction can be accomplished by choosing a spectral truncation that excludes barotropic instability by triad interactions. Such a choice is possible because of Fjørtoft's theorem (1953). This theorem states that there can be no energy and enstrophy transport in one direction of the wave spectrum. Therefore the only unstable triads are those satisfying the following inequality for total wave number n:

$$n_\alpha < n_\gamma < n_\beta, \tag{4}$$

where the subscript γ denotes the primary wave and α and β the perturbations. The spectral truncation used in this section is shown in Fig. 1. The crosses indicate the vorticity components, whereas the divergence and geopotential are denoted by circles. The spherical harmonics retained in this spectral truncation are the zonal modes (0, 1) and (0, 3), and the wave modes (2, 3) and (2, 5). Because of (4), barotropic instability is impossible for these modes. The interaction of the wave modes with the (0, 1) mode is forbidden, because the (0, 1) mode represents the total angular momentum, which is a conservative quantity in the absence of friction and topography. The only possible type of self-resonance is long-wave/short-wave resonance, which occurs for a zonal flow configuration with stationary eigenmodes. This results in resonant decay of the eigenmodes, transporting energy into the zonal flow. Second harmonic resonance is impossible because of the absence of modes with $m = 4$.

The vorticity equation (1a) is forced in the (0, 1) and (2, 3) component:

$$G_{\mathrm{f}} = \zeta_1^{0*} P_1^0(\lambda, \mu) + \zeta_3^{2*} P_3^2(\lambda, \mu). \tag{5}$$

Here $P_n^m(\lambda, \mu)$ is the associated Legendre polyno-

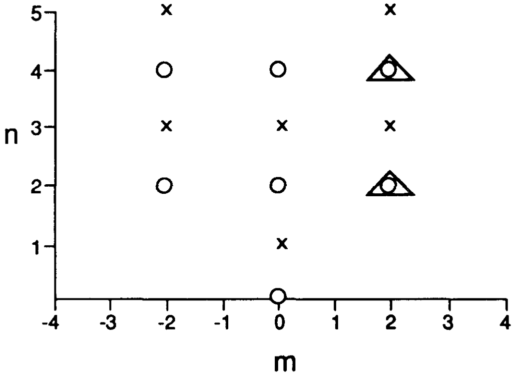

Fig. 1. Spectral truncation of the shallow water equations. The vorticity components are indicated by crosses, the divergence and geopotential by circles. The topography is denoted by a triangle.

mial, where λ is longitude, $\mu = \sin\phi$ and ϕ is latitude. The coefficient ζ_n^{m*} denotes the strength of the forcing in the (m, n) component. The steady states were computed for increasing ζ_1^{0*}, keeping ζ_3^{2*} at a fixed value. This was done for $\zeta_3^{2*} = 1.4 \cdot 10^{-2}$ and $\zeta_3^{2*} = 5.6 \cdot 10^{-2}$. These values correspond with a maximum vorticity forcing at 35°N of $0.74 \cdot 10^{-10}\,s^{-2}$ and $2.96 \cdot 10^{-10}\,s^{-2}$ respectively. Although the former forcing is in the order of 200 m day^{-1}, which is not really weak, we will for convenience denote these two wave forcings as weak and strong wave forcing respectively. For the computation of steady states we used the pseudo-arclength method as described by Legras and Ghil (1985).

Fig. 2 displays the projection of the steady-state curves on the (2, 3) vorticity component for weak wave forcing (curve a) and strong wave forcing (curve b). The weak wave forcing curve shows a peak at $\zeta_1^{0*} = 0.78 \cdot 10^{-2}$. For this value of ζ_1^{0*}, the strength of the (0, 1) component in the solution is 0.30. This is the value for which the "(2, 3)" eigenmode (one of the two eigenvectors of the zonal symmetric part of the steady state) becomes stationary, resulting in resonant excitation of this mode by the wave forcing ζ_3^{2*}. The (0, 3) component (not shown) of all computed steady states remains very small ($<0.3 \cdot 10^{-2}$), the energy transfer from the "(2, 3)" mode to the zonal modes due to self-interaction is balanced by the dissipation. Bifurcations do not occur for weak wave forcing; all computed steady states are stable.

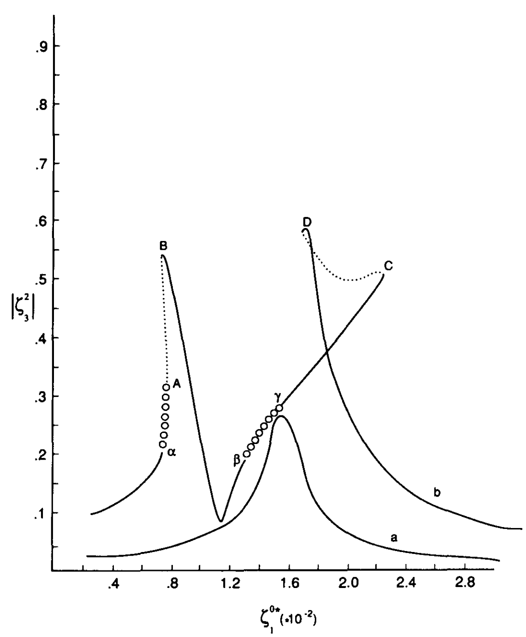

Fig. 2. Projection of the steady state curves on $|\zeta_3^2|$ for $\zeta_3^{2*} = 1.4 \cdot 10^{-2}$ (curve a) and $\zeta_3^{2*} = 5.6 \cdot 10^{-2}$ (curve b). $F = 2.75$. Dots indicate unstable steady states with a positive real eigenvalue. Unstable steady states possessing a pair of complex conjugated eigenvalues with a positive real part are denoted by a circle.

The results for strong wave forcing (curve b of Fig. 2) show significant differences with those for weak wave forcing. The projection of the steady-state curve on the (2, 3) vorticity component now displays two peaks instead of one. Both peaks are folded, resulting in multiple steady states for ζ_1^{0*} between $0.37 \cdot 10^{-2}$ and $0.39 \cdot 10^{-2}$ and between $0.86 \cdot 10^{-2}$ and $1.13 \cdot 10^{-2}$. In contrast with the weak forcing case the (0, 3) component (not shown) now attains a considerable amplitude with maxima in the order of 0.6.

At the turning points (points A, B, C and D) a saddle-node bifurcation occurs, where a real eigenvalue changes sign. The steady states and the returning branches of the curve (between A and B, and C and D) are unstable, possessing a single real and positive eigenvalue. The stationary growing perturbations display contributions from the zonal as well as the wave components.

Hopf bifurcations occur at the points α, β and γ. At point A a Hopf and a saddle-node bifurcation occur very close to each other. Like the growing perturbations due to the saddle-node bifurcations, the limit cycles due to the Hopf bifurcations display contributions from the zonal as well as the wave components.

5. Bifurcations in a model with topographic instability and self-interaction

In this section, we investigate how the introduction of self-interaction affects the bifurcation diagram that originates from topographic instability. First, in Subsection 5.1, we compute the steady states for a model with topographic instability only. Subsequently we compute in Subsection 5.2 the steady states when self–interaction is included. In that section we also present an analysis of the observed differences between the steady-state curves of these two experiments.

5.1. Topographic instability

In order to exclude self-interaction, we set F at a very small value ($F = 10^{-5}$). The spectral truncation is the same as used in the previous experiment. The topography is represented by the (2, 2) and (2, 4) components. They are indicated by triangles in Fig. 1. We choose $\eta_2^2 = 0.122$ and $\eta_4^2 = 0.077$. This results in a mountain with zonal wave number two and a meridional structure such as depicted in Fig. 3. The maximum amplitude of η is 0.2, which is attained at 43°N. The possible interactions between the topography and the wave components are given below:

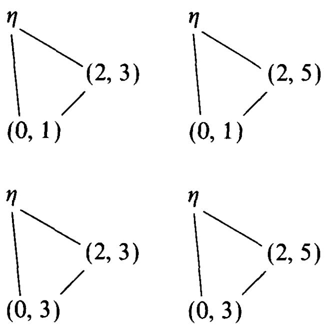

Due to the topography energy flows from the zonal into the wave components and vice versa.

In contrast to the previous experiment with self-interaction, the vorticity equation (1a) is only forced in the (0, 1) component:

$$G_f = \zeta_1^{0*} P_1^0(\lambda, \mu). \tag{6}$$

No forcing is applied at the (2, 3) component. The wave modes are solely excited by interaction of the zonal flow with the topography. We have computed the steady states for increasing ζ_1^{0*}. The projection of the steady-state curve on the (0, 1) component of the vorticity is shown in Fig. 4. It displays a number of folds or saddle-node bifurcations. The three folds where the steady-state curve returns are indicated by I, II and III. The returning branches of the curve are unstable, possessing a single real and positive eigenvalue. Due to the folds in the steady-state curve, at least three steady states exist simultaneously between $\zeta_1^{0*} = 1.54 \cdot 10^{-2}$ and $\zeta_1^{0*} = 3.48 \cdot 10^{-2}$ and five between $\zeta_1^{0*} = 0.64 \cdot 10^{-2}$ and $\zeta_1^{0*} = 0.90 \cdot 10^{-2}$. The amplitudes of the (2, 3) and (2, 5) component (not shown) display local maxima at II and I respectively, whereas both components attain their absolute maximum close to III. At this point both components are approximately 90° out of phase with the topography, resulting in a large form drag. For ζ_1^{0*} larger than $1.9 \cdot 10^{-2}$, beyond the last fold in the steady-state curve, both components are approximately in phase with the

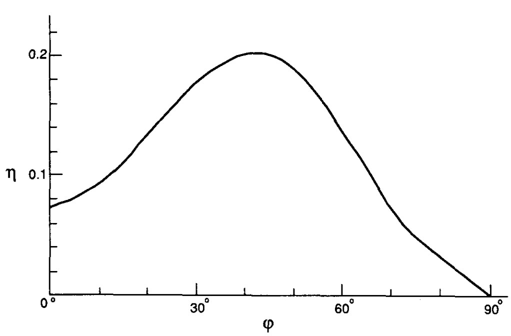

Fig. 3. Meridional structure of the topography.

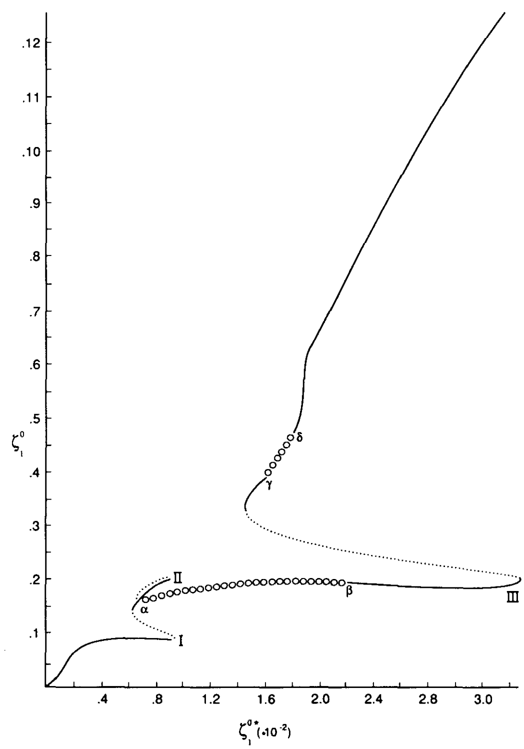

Fig. 4. Projection of the computed steady state curve on ζ_1^0 for $F = 1 \cdot 10^{-5}$. The symbols indicating the stability of the steady states are the same as in Fig. 2.

topography. For these states the form drag is small, and consequently an increment of ζ_1^{0*} mainly results in an increment of ζ_1^0.

Hopf bifurcations are observed after the second and third fold at $\zeta_1^{0*} = 0.71 \cdot 10^{-2}$ (point α) and $\zeta_1^{0*} = 1.63 \cdot 10^{-2}$ (point γ), resulting in growing perturbations between α and β, and γ and δ.

5.2. *Topographic instability and self-interaction*

In order to allow self-interaction we now choose $F = 2.75$, and repeat the experiment of the foregoing section. We will refer to the experiment with $F = 2.75$ as B and to the experiment of the previous section as A.

The projection of the steady-state curve on the (0, 1) vorticity component is displayed in Fig. 5. Comparison with the steady-state curve for experiment A (Fig. 4) shows that for ζ_1^{0*} smaller than $1.3 \cdot 10^{-2}$ both curves are very similar. This is also the case for the (2, 3) and (2, 5) components (not shown). The folds I and II occur for approximately the same values of ζ_1^{0*}. Significant differences exist for larger values of ζ_1^{0*}. In B, fold III occurs for a much smaller value of ζ_1^{0*} ($1.32 \cdot 10^{-2}$). The peaks in the (2, 3) and (2, 5) components at this bifurcation point are also much smaller than in experiment A. Apparently at larger values of ζ_1^{0*} self-interaction facilitates the formation of bifurcations due to topographic instability, by transferring topographically induced wave energy back into the zonal flow component. For still larger values of ζ_1^{0*} a completely new fold in the steady-state curve appears at $\zeta_1^{0*} = 2.0 \cdot 10^{-2}$ (IV).

The Hopf bifurcation in experiment A, after the second fold disappears, whereas the Hopf bifurcation after the third fold now occurs at $\zeta_1^{0*} = 0.95 \cdot 10^{-2}$ (point γ) resulting in growing perturbations for ζ_1^0 between $0.95 \cdot 10^{-2}$ and $1.13 \cdot 10^{-2}$ (point δ).

The introduction of self-interaction thus causes significant changes in the steady-state curve of experiment A. In order to investigate the relative contribution of both topographic instability and self-interaction for each of the bifurcations in the new steady-state curve, we performed a stability analysis of the steady states for the linearized equations without the topographic term. The result is shown in Fig. 6. The steady states on the returning branches of folds I and III are all stable, while the states on the returning branch of II are only par-

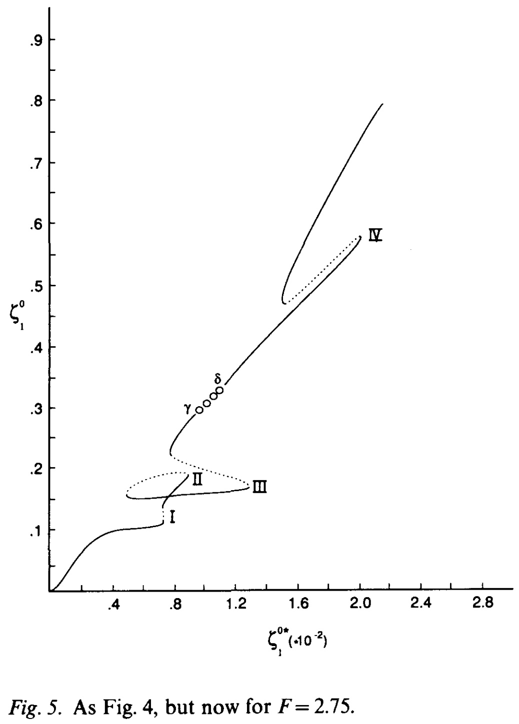

Fig. 5. As Fig. 4, but now for $F = 2.75$.

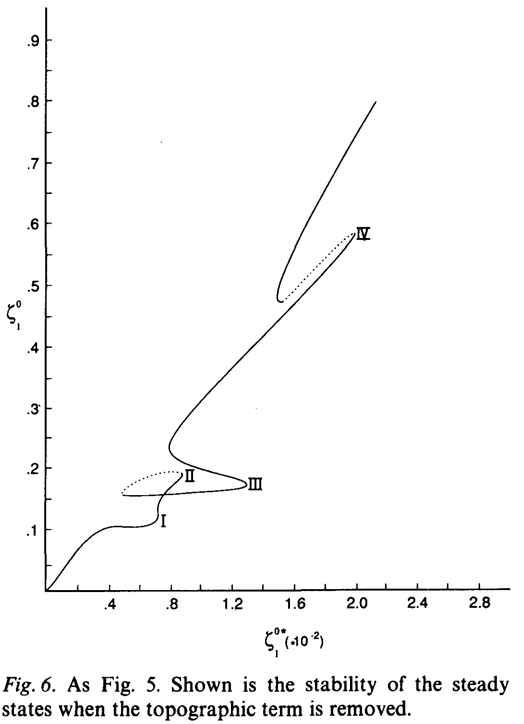

Fig. 6. As Fig. 5. Shown is the stability of the steady states when the topographic term is removed.

tially unstable, displaying much smaller growth rates than the original ones. From this we conclude that these three folds originate from topographic instability. The topographic origin of the first two folds is in agreement with the already observed fact that the steady-state curve for small ζ_1^{0*} is very similar to the one in experiment A, with topographic instability only. Also the third fold, although significantly modified by self-interaction still originates from topographic instability. The growth rates on the returning branch of fold IV hardly change when the topographic term is removed. This new fold is thus caused by self-interaction. The Hopf bifurcation beyond III at $\zeta_1^{0*} = 0.95 \cdot 10^{-2}$ has disappeared revealing that the origin of this bifurcation is of a topographic nature.

In order to obtain a better understanding of the changes in the steady-state curve caused by the introduction of self-interaction, we will use Pedlosky's (1981) analysis of topographic instability. In the analysis of Pedlosky, which is valid when $\eta^{1/3} \ll 1$, the structure of the topographically forced wave is approximately equal to that of a free wave. The nonlinear interactions only determine the amplitude of the wave. Folds in the steady state curve occur when the zonal flow is slightly stronger than the zonal flow for which a free wave is stationary (super resonant flow) (Figs. 1, 2 of his paper). In Pedlosky's analysis the zonal flow is only in second order affected by the nonlinear interactions. In our experiment, where $\eta = 0.2$, the forced zonal flow component is strongly modified by interactions; the amplitude of the (0, 3) component is comparable to that of the (0, 1) component. Despite the strong nonlinearities, we will apply his analysis to our results.

We computed the frequency ω of the eigenmodes of the zonal symmetric part of the computed steady states. The structure of the eigenmodes changes constantly along the steady-state curve, but they can always be identified. For the BVE in solid body rotation they reduce to the spherical harmonics (2, 5) and (2, 3). In the following, we shall denote these modes as mode 1 and mode 2 respectively. Fig. 7a displays for experiment A ($F = 1 \cdot 10^{-5}$) the frequencies of mode 1 (curve α) and mode 2 (curve β) as a function of the (0, 1) vorticity component of the computed steady states. The arrows I, II and III indicate the posi-

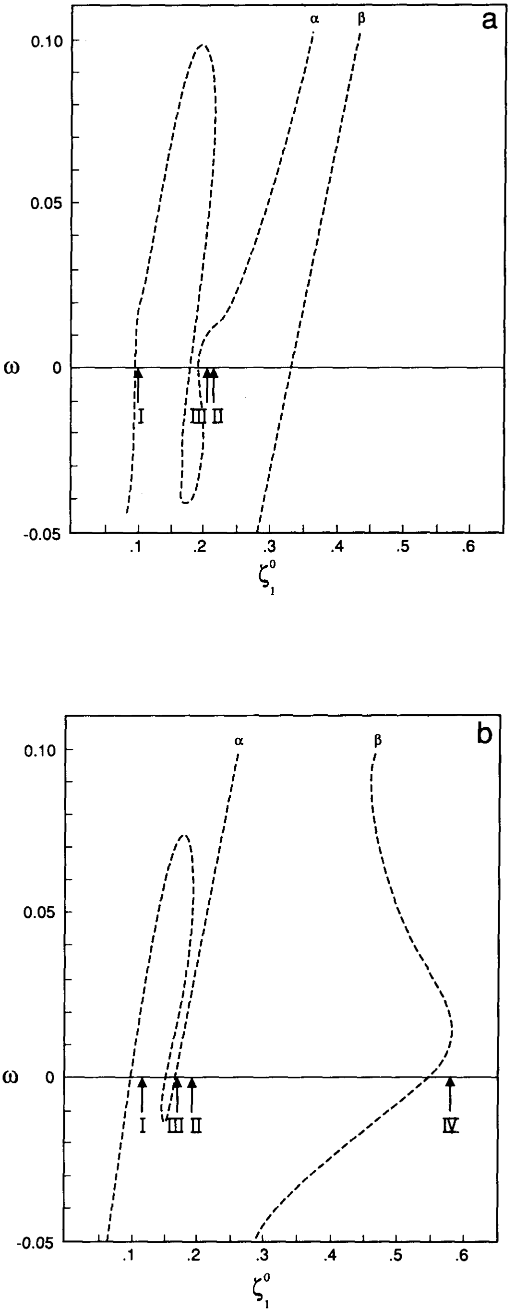

Fig. 7. Frequencies of the modes of the zonal symmetric part of the computed steady states for $F = 1 \cdot 10^{-5}$ (a) and $F = 2.75$ (b). The frequencies are displayed as a function of ζ_1^0 of the computed steady states. The arrows indicate the saddle node bifurcations.

tion of the folds where the steady-state curve returns. Mode 1 becomes stationary for $\zeta_1^0 = 0.093$, which is somewhat smaller than 0.095 for which the first folds occurs.

In agreement with the analysis of Pedlosky, this fold thus occurs for slightly super resonant flow. This mode is also stationary for $\zeta_1^0 = 0.175$ and $\zeta_1^0 = 0.192$. Again these values are somewhat smaller than the values of ζ_1^0 for which the other two folds occur: $\zeta_1^0 = 0.209$ (II) and $\zeta_1^0 = 0.200$ (III). It follows that all three folds in the steady-state curve occur when mode 1 is super resonant. Mode 2 is stationary for $\zeta_1^0 = 0.327$. However, the steady-state curve does not show a corresponding fold. In this case the Rayleigh friction is too strong in comparison with the topographic forcing for bifurcations to occur.

The frequencies of the two modes for experiment B are displayed in Fig. 7b. Similarly as for experiment A the first three folds in the steady-state curve, which originate from topographic instability, are connected to super resonance of mode 1. The values of ζ_1^0 for which this mode becomes stationary, i.e., 0.104, 0.153 and 0.167 are approximately the same as in experiment A.

The new fold (IV) occurs at $\zeta_1^0 = 0.578$, which is somewhat larger than the value for which mode 2 becomes stationary ($\zeta_1^0 = 0.545$). In contrast to experiment A, the introduction of self-interaction thus causes a fold when mode 2 is super-resonant.

Compared to experiment A, mode 2 becomes stationary for a much larger value of ζ_1^0, because, the frequency of this mode does not increase linearly with ζ_1^0. Self-interaction thus strongly influences the frequency of mode 2 by feeding back wave energy into the (0, 3) component of the zonal flow, thereby altering the frequency and structure of the eigenmodes of this zonal flow. Fig. 8, displaying the projection of the steady-state curve on the (0, 3) vorticity component for experiment A and B, clearly shows the large differences in the amplitude of this component between A and B. In experiment A the ζ_3^0 component decreases rapidly after fold III, whereas in experiment B, this component strongly increases with ζ_1^{0*} until fold IV. For large values of ζ_1^{0*} self-interaction thus completely changes the distribution of energy between zonal and wave components.

Fig. 8 shows that in both experiments the value of ζ_3^0 is approximately the same for the first three folds. This is also the case for the (0, 1) component

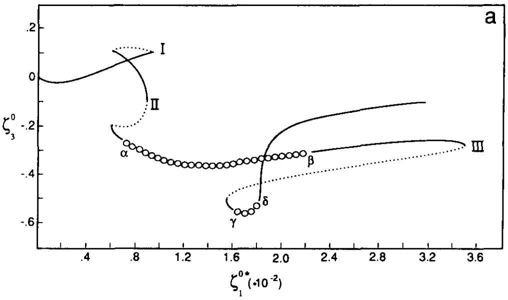

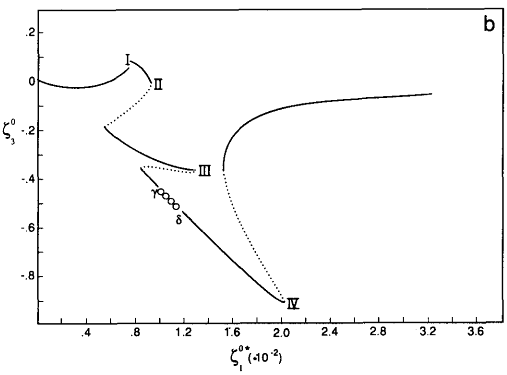

Fig. 8. Projection of the computed steady-state curve on ζ_3^0 for $F = 1 \cdot 10^{-5}$ (a) and $F = 2.75$ (b).

(Fig. 7). The reduction in ζ_1^{0*} for which fold III occurs in experiment B, is thus connected to the smaller amplitudes of the wave components of the steady states. As discussed before, this reduction is caused by self-interaction which feeds back energy from the waves into the zonal flow, preventing the existence of steady states with large wave amplitudes.

Summarizing, we state that for small ζ_1^{0*} self-resonance does not significantly affects the steady-state curve originating from topographic instability. For larger values of ζ_1^{0*} ($> 1.3 \cdot 10^{-2}$), self-interaction significantly reduces the value of ζ_1^{0*} for which fold III occurs. A new fold, entirely caused by self-interaction, emerges for still larger values of ζ_1^{0*}. In agreement with the quasi-linear theory of Pedlosky we demonstrated that, although in our experiment the flow is highly non-linear, folds due to topographic instability as well as self-interaction occur when the zonal flow is slightly super resonant.

6. Conclusions and discussions

The shallow-water equations including topography contain three instability mechanisms, i.e., topographic instability, barotropic instability and self-interaction. In Haarsma and Opsteegh (1988) the last two instability mechanisms were investigated. There it was shown that they can be described by triad and dyad interactions respectively and that the critical amplitudes for instability as well as the growth rate and frequency of the growing perturbations depend on Lamb's parameter F. For $F=0$, in which case the shallow-water equations reduce to the barotropic vorticity equation, self-interaction is impossible.

The effect of topographic instability on the bifurcation diagram was first studied by Charney and DeVore (1979). For a low-order model, they demonstrated the possibility of saddle-node bifurcations due to topographic instability. Others have studied the effect of barotropic instability (Källén, 1981; Legras and Ghil, 1985) and baroclinic instability (Charney and Straus, 1980; Reinhold and Pierrehumbert, 1982).

Following these studies, we have analyzed the bifurcation diagram in a low-order model with self-interaction. We investigated how the introduction of self-interaction affects the bifurcation diagram which originates from topographic instability. For small ζ_1^{0*} self-interaction does not significantly affect the steady-state curve originating from topographic instability. Significant changes appear for ζ_1^{0*} larger than $1.3 \cdot 10^{-2}$. In absence of topography, this value of ζ_1^{0*} would result in a zonal flow of about $100\,\mathrm{m\,s^{-1}}$ at midlatitude. For the atmosphere this is an unrealistically large value. Whether or not self-interaction is important for the real atmosphere remains unclear. This can only be answered by investigating more realistic models of the atmosphere.

REFERENCES

Benzi, R., Malguzzi, R., Speranza, A. and Sutera, A. 1986. The statistical properties of general atmospheric circulation: observational evidence and a minimal theory of bimodality. *Quart. J. R. Met. Soc. 112*, 661–674.

Boyd, J. P. 1983a. Long wave/short wave response in equatorial waves. *J. Phys. Oceanogr. 13*, 450–458.

Boyd, J. P. 1983b. Second harmonic resonance for equatorial waves. *J. Phys. Oceanogr. 13*, 459–466.

Charney, J. G. and DeVore, J. G. 1979. Multiple flow equilibria in the atmosphere and blocking. *J. Atmos. Sci. 36*, 1205–1216.

Charney, J. G. and Straus, D. M. 1980. Form-drag instability, multiple equilibria and propagating planetary waves in baroclinic orographically forced planetary wave systems. *J. Atmos. Sci. 37*, 1157–1176.

Fjørtoft, R. 1953. On the changes in the spectral distribution of kinetic energy for two dimensional, nondivergent flow. *Tellus 5*, 225–230.

Haarsma, R. J. and Opsteegh, J. D. 1988. Barotropic instability of planetary-scale flows. *J. Atmos. Sci. 45*, 2789–3016.

Källén, E. 1981. The nonlinear effects of orographic and momentum forcing in a low-order barotropic model. *J. Atmos. Sci. 38*, 2150–2163.

Legras, B. and Ghil, M. 1985. Persistent anomalies, blocking and variations in atmospheric predictability. *J. Atmos. Sci. 42*, 433–471.

Longuet-Higgins, M. S. 1968. The eigenfunctions of Laplace's tidal equations over a sphere. *Proc. R. Soc., London, Ser. A. 262*, 511–607.

Pedlosky, J. 1981. Resonant topographic waves in barotropic and baroclinic flows. *J. Atmos. Sci. 38*, 2626–2641.

Reinhold, B. B. and Pierrehumbert, R. T. 1982. Dynamics of weather regimes: Quasi-stationary waves and blocking. *Mon. Wea. Rev. 110*, 1105–1145.